Journal of Marine Research, 59, 567–597, 2001

The origin of low-frequency variability of double-gyre wind-driven flows

by Janine J. Nauw[1] and Henk A. Dijkstra[1]

ABSTRACT

Bifurcation analysis on flows in a two-layer shallow-water model is used to clarify the dynamical origin of low-frequency variability of the double-gyre wind-driven ocean circulation. In many previous model studies, generic low-frequency variations appear to be associated with distinct regimes, characterized by the level of kinetic energy of the mean flow. From these transient flow computations, the current view is that these regimes, and transitions between them, arise through a complex nonlinear interaction between the mean flow and its high-frequency instabilities (the eddies). On the contrary, we demonstrate here, for a particular (but relevant) case, that the origin of these high- and low-energy states is related to the existence of low-frequency instabilities of steady-state flows. The low-frequency modes have distinct spatial patterns and introduce preferential patterns oscillating on interannual to decadal time scales into the flow. In addition, these low-frequency modes are shown to be robust to the presence of (idealized) topography; the latter may even have a destabilizing effect.

1. Introduction

The existence of low-frequency variability in the North-Atlantic climate has been demonstrated through many observational studies; for example, in large-scale sea surface temperature (SST) and sea-level pressure patterns (Deser and Blackmon, 1993; Kushnir, 1994; Levitus, 2000). There is currently debate on whether internal variability of the ocean circulation significantly contributes to the large-scale climate fluctuations on interannual to interdecadal time scales. On the interdecadal time scale, the ocean seems to be in a good position since preferred spatio/temporal patterns arise through instabilities of the thermohaline circulation (Huck *et al.,* 1999; Colin de Verdière and Huck, 1999; Te Raa and Dijkstra, 2001). However, both observational and model studies indicate that variability on the interannual time scale can probably be totally accounted for by variability of the atmosphere coupled to a more or less dynamically passive ocean (Delworth, 1996). The decadal time scale variability possibly can be viewed as an intermediate case, where both the atmosphere as well as the ocean are dynamically involved (Latif and Barnett, 1994).

Complication to this picture arises because many model studies have indicated that the

1. Institute for Marine and Atmospheric Research, Department of Physics and Astronomy, Utrecht University, Princetonplein 5, 3584 CC Utrecht, The Netherlands ***email: j.j.nauw@phys.uu.nl***

ocean circulation displays internal variability on subannual to decadal time scales; i.e., on time scales larger than those arising through mesoscale eddy activity (Cox, 1987; Miller *et al.,* 1987). A prototype model for this problem is a wind-driven, single- or double-gyre flow in a rectangular basin. Basically, both situations are extreme cases of the 'real' North Atlantic situation, with the single-gyre model completely neglecting the subpolar gyre and the double-gyre model overestimating its presence. Most of the studies have used the traditional methods of computing transient flows at several values of parameters and determining statistical properties of the resulting complex flows. For example, EOF analysis is used to determine dominant patterns of variability and spectra of time series of characteristic quantities (McWilliams, 1996) are calculated.

In a two-layer quasi-geostrophic model with a symmetric double-gyre forcing, Berloff and McWilliams (1999) compute trajectories for five values of the lateral friction coefficient, A_H, for a flow in a basin of realistic size. For the highest value of the friction ($A_H = 1200\ \mathrm{m^2\,s^{-1}}$), a nonsymmetric steady state is found. When lateral friction is decreased, the flow first displays variability at particular frequencies and with distinct variability patterns. At $A_H = 1000\ \mathrm{m^2\,s^{-1}}$, quasi-periodic variability is found with dominant frequencies in the intermonthly and interannual range, which correspond to those found in a 1.5-layer model for a similar value of the friction. At smaller friction, a more or less broader spectrum appears with increased energy in the low-frequency range. At $A_H = 800\ \mathrm{m^2\,s^{-1}}$, the behavior of the time series is termed 'chaotic' and at $A_H = 600\ \mathrm{m^2\,s^{-1}}$, the flow seems to be concentrated near three states with different total energy. These states are characterized by a different penetration length of the eastward jet and the presence or absence of oscillations with dipole-type patterns. Similar low-frequency behavior is found in the study of McCalpin and Haidvogel (1996), using a quasi-geostrophic model. The 'quasi' stable high-energy periods show a free jet, extending far into the basin, which is hardly showing any meanders and on which only weak eddies are formed. The low-energy state is characterized by extensive meandering and eddy formation in the region just beyond the separation point, so that the existence of a free jet is not always obvious. The dynamical view they provide is rather descriptive but the central ingredient is 'eddy-jet' interaction, which is responsible for formation of rings and evolution of meanders.

Without any further analysis techniques of the dynamical behavior of the flow, the origin of this low-frequency variability of western boundary currents and midlatitude jets would remain obscure. This understanding is now developing and has been initiated by bifurcation studies, which have determined the structure of steady states and large-scale instabilities in idealized models (Cessi and Ierley, 1995; Jiang *et al.,* 1995; Speich *et al.,* 1995; Dijkstra and Katsman, 1997; Primeau, 1998; Chang *et al.,* 2001; Simonnet *et al.,* 2001a, b; Simonnet and Dijkstra, 2001). For example, it has been shown that asymmetric steady states exist through spontaneous symmetry breaking and that the first Hopf bifurcations introduce intermonthly and interannual variability. Usually, only the first couple of Hopf bifurcations are determined and the periodic orbit arising from the first Hopf bifurcation is followed (Dijkstra, 2000). In fact, Berloff and McWilliams (1999) heavily use the

knowledge of this dynamically (fairly robust) picture to interpret their results at high friction, but in the very small friction regime turn to more traditional interpretations by lack of the knowledge of the route to complexity in these flows. In the latter regime, they find no direct relationship between the patterns of the low-frequency flow and the patterns which destabilize the steady state at the Hopf bifurcations. Although not explicitly stated, this may suggest to modelers that analysis of the first couple of bifurcations does not help to explain the flows in the 'realistic' regime.

Here, bifurcation analysis and trajectory computation are used to aim to clarify the relation between the sequence of Hopf bifurcations and low-frequency behavior which is associated with high- and low-energy states. As a first step, a weakly to mildly nonlinear (relatively small basin/low forcing) regime is considered within a two-layer shallow-water model context. The spectrum of the double-gyre flows in this model shows instability of all the interesting modes over a reasonable range of the wind stress strength. It is shown that low-frequency variability is associated with the destabilization of asymmetric steady states to a particular (low-frequency) mode. Although this mode is damped at the first Hopf bifurcation, it plays a major role in the transient flow at stronger forcing (or lower friction) by being responsible for the transitions between high- and low-energy states. To demonstrate that this is not solely characteristic for the flat-bottom case, the modes are shown to be robust to the presence of two (idealized) types of bottom topography.

2. Model and methods

The two-layer shallow-water equations are solved in a rectangular basin with horizontal dimensions of 1000 × 2000 km located on a β-plane centered at 45N. Bottom topography may be present giving a total depth of $H_0 - H_b(x, y)$, where H_0 represents the constant depth in the flat bottom case.

a. Description of the model

Both layers have a constant density ρ_1 and ρ_2, with $\rho_2 > \rho_1$. Laplacian lateral friction is present with (eddy) lateral mixing coefficient A_H. The flow is driven by a stationary wind stress pattern (τ_1^x, τ_1^y). For each layer $i = 1, 2$, the governing equations are (Holland and Lin, 1975)

$$\frac{\partial U_i}{\partial t} + \nabla \cdot (\mathbf{u}_i U_i) - fV_i = -\frac{h_i}{\rho_0}\frac{\partial p_i}{\partial x} + A_H h_i \nabla^2 u_i + \frac{\tau_i^x}{\rho_0} \tag{1a}$$

$$\frac{\partial V_i}{\partial t} + \nabla \cdot (\mathbf{u}_i V_i) + fU_i = -\frac{h_i}{\rho_0}\frac{\partial p_i}{\partial y} + A_H h_i \nabla^2 v_i + \frac{\tau_i^y}{\rho_0} \tag{1b}$$

$$\frac{\partial h_i}{\partial t} + \nabla \cdot \mathbf{U}_i = 0 \tag{1c}$$

Table 1. Standard values of the dimensional parameters in the two-layer shallow-water model. The wind stress amplitude τ_0 will be used as control parameter.

Parameter	Value	Parameter	Value
L	$1.0 \cdot 10^6$ m	D	$2.0 \cdot 10^6$ m
g	9.8 m s^{-2}	ρ_0	$1.0 \cdot 10^3$ kg m^{-3}
R	$5.0 \cdot 10^{-8}$ s^{-1}	A_H	$3.0 \cdot 10^2$ m^2 s^{-1}
f_0	$1.0 \cdot 10^{-4}$ s^{-1}	β_0	$1.8 \cdot 10^{-11}$ m^{-1} s^{-1}
ρ_1	$1.0 \cdot 10^3$ kg m^{-3}	ρ_2	$1.002 \cdot 10^3$ kg m^{-3}
H_1	$7.0 \cdot 10^2$ m	H_2	$3.3 \cdot 10^3$ m

where $U_i = u_i h_i$ and $V_i = v_i h_i$ are the volume fluxes per unit length, (u_i, v_i) the zonal and meridional velocities and h_i is the thickness of layer i. In the β-plane approximation, $f = f_0 + \beta_0 y$, f_0 is the Coriolis parameter and β_0 is the local meridional derivative of f. The rigid-lid approximation and the condition of continuity of normal stress at the interface of the layers become

$$h_1 + h_2 = H_0 - H_b(x, y) \tag{2a}$$

$$\nabla p_2 = \nabla p_1 - \rho_0 g' \nabla h_1 \tag{2b}$$

The reduced gravity is defined by $g' = g(\rho_2 - \rho_1)/\rho_0$, where ρ_0 is a reference density. No-slip boundary conditions are applied at all lateral walls. The standard values of the parameters can be found in Table 1 and are similar to those used in Speich *et al.* (1995). The equilibrium depth of each layer in the flat bottom case is indicated by H_1 and H_2.

The stress term in the right-hand side of Eqs. (1a, b) represents the wind stress forcing in the top layer and a bottom friction in the second layer. For the top layer, a double-gyre wind stress is chosen

$$\tau_1^x = -\tau_0 \cos(2\pi y/D) \tag{3a}$$

$$\tau_1^y = 0 \tag{3b}$$

and for the second layer, we took a linear bottom friction, i.e.

$$\tau_2^x = -\rho_0 R U_2 \tag{4a}$$

$$\tau_2^y = -\rho_0 R V_2. \tag{4b}$$

There is no interfacial friction and hence in steady state, the lower layer is motionless. Nonzero flow in the lower layer can only occur through transient effects such as the presence of, and interaction between, baroclinic instabilities (Pedlosky, 1996).

The wind stress amplitude τ_0 will be used as a control parameter, while the values of the friction coefficients remain fixed. Reason for choosing the relatively small basin is that the instabilities and location of the steady state branches are well known for the 1.5-layer set-up (Speich *et al.,* 1995) and provide an easy starting point. The small basin size is not

expected to have much effect on the dynamical picture, because bifurcation diagrams for 1.5-layer models with larger basin sizes and even with full continental geometry are qualitatively similar to those of a small rectangular basin (Dijkstra and Molemaker, 1999; Schmeits and Dijkstra, 2001).

b. Numerical methods

After discretizing the equations on an Arakawa C-grid, two different numerical methodologies are used: standard transient flow computation and bifurcation analysis. The standard resolution used is $\Delta x = \Delta y = 20$ km, similar to that in Jiang *et al.* (1995) and Speich *et al.* (1995). An estimate of the Munk boundary layer thickness $(A_H/\beta_0)^{1/3}$ calculated with the use of Table 1 is about 25 km. This resolution is sufficient to resolve the flows in the parameter regime considered. For example, there is a close resemblance between the patterns of the eigenmodes and the positions of the first Hopf bifurcations of Speich *et al.* (1995), who also used a resolution of 20 km, and in Dijkstra and Molemaker (1999) where a very high resolution in the western boundary layer is used.

To compute transient flows, the traditional method of integrating forward in time with the leap-frog method is used (with a timestep $\Delta t = 30$ min), similar to that in Holland (1973). The computational mode of the leap-frog scheme is damped with a three-point time smoother (Asselin, 1972) on the components of the velocity (u_i, v_i) and on the layer thicknesses (h_i) and the rigid-lid approximation is implemented in a similar way as in Bleck and Boudra (1981).

To perform bifurcation analysis, the continuation techniques as described in Schmeits and Dijkstra (2001) are used. Since the latter techniques are not (yet) standard, a short description is given (for an extensive description, see Dijkstra (2000)). Steady-state solutions of the equations satisfy a set of nonlinear algebraic equations of the form:

$$\mathbf{F}(\mathbf{u}, \mathbf{p}) = 0. \tag{5}$$

Here $\mathbf{u}$ is the d-dimensional vector consisting of the unknowns (velocities, layer thicknesses and pressures) at the grid points and $\mathbf{p}$ is the p-dimensional vector of parameters. To determine branches of steady solutions of the equations as one of the parameters (say μ) is varied, the pseudo-arclength method is used. The branches $(\mathbf{u}(s), \mu(s))$ are parameterized by an 'arclength' parameter s. An additional equation is obtained by 'normalizing' the tangent

$$\dot{\mathbf{u}}_0^T(\mathbf{u} - \mathbf{u}_0) + \dot{\mu}_0(\mu - \mu_0) - \Delta s = 0 \tag{6}$$

where $(\mathbf{u}_0, \mu_0)$ is an analytically known starting solution or a previously computed point on a particular branch and Δs is the steplength. The system (5, 6) is solved by the Newton-Raphson method.

When a steady state is determined, the linear stability of the solution is considered and transitions that mark qualitative changes, such as transitions to multiple equilibria (pitchfork or saddle node bifurcations) or periodic behavior (Hopf bifurcations), can be

detected. The linear stability analysis amounts to solving a generalized eigenvalue problem of the form

$$\mathcal{A}\mathbf{x}=\sigma\mathcal{B}\mathbf{x} \tag{7}$$

where $\mathcal{A}$ and $\mathcal{B}$ are nonsymmetric matrices. Bifurcations are detected from crossings of the eigenvalue $\sigma = \sigma_r + i\sigma_i$ with the imaginary axis. Solution techniques for these problems are presented in Dijkstra (2000). Here, the problem is solved with the Simultaneous Iteration Method (Steward and Jennings, 1981) and only a few of the most unstable/least stable modes (with σ_r near zero) are calculated.

3. Results

The results are presented along the following path. First, the flat bottom case is considered and the basic steady state structure is computed. This will be an imperfect pitchfork bifurcation as in the 1.5-layer case (Speich *et al.,* 1995), because the bottom layer is motionless for steady flows. However, in the two-layer model new instabilities appear through baroclinic physics (Section 3a) and their relation with the transient flows is analyzed in Section 3b. Subsequently, the influence of two particular types of bottom topography is considered (Section 3c).

a. Basic bifurcation diagram: Flat bottom case

With a flat bottom, the equilibrium layer thicknesses are $H_1 = 700$ m and $H_2 = 3300$ m as shown in Table 1, giving a total thickness $H_0 = 4000$ m. Steady states are computed, using τ_0 as a control parameter and as a norm of the solution the minimum upper layer thickness, $h_{1,\min}$, is plotted. In Figure 1 the drawn (dashed) lines represent stable (unstable) steady states. An imperfect pitchfork bifurcation is found with a unique steady solution for values below $\tau_0 = 6.7 \times 10^{-2}$ Pa and multiple steady states beyond this value.

Along the upper branch in Figure 1, the results of the linear stability analysis indicate that the steady state becomes unstable through a sequence of Hopf bifurcations (indicated by triangular markers). The stability of the isolated branch has not been calculated because it is expected that the Hopf bifurcations which appear on this branch have similar patterns and frequencies as those on the upper branch, as in the 1.5-layer case (Dijkstra and Molemaker, 1999). Moreover, it has been found from the computations of the transient flows (Section 3b below) that only at some locations in parameter space, signatures of the instabilities of the lower branch of steady states are noticeable. Hence, these instabilities are not considered in further detail.

At each Hopf bifurcation, a complex conjugate pair of eigenvalues $\sigma = \sigma_r \pm i\sigma_i$ crosses the imaginary axis. The corresponding eigenvector $\mathbf{x} = \mathbf{x}_R + i\mathbf{x}_I$ (obtained from (7)) provides the spatial pattern of the mode which destabilizes the steady state. The time-dependent behavior of this mode $\mathbf{P}(t)$ locally near the Hopf bifurcation is given by

$$\mathbf{P}(t) = e^{\sigma_r t}[\mathbf{x}_R \cos(\sigma_i t) - \mathbf{x}_I \sin(\sigma_i t)] \tag{8}$$

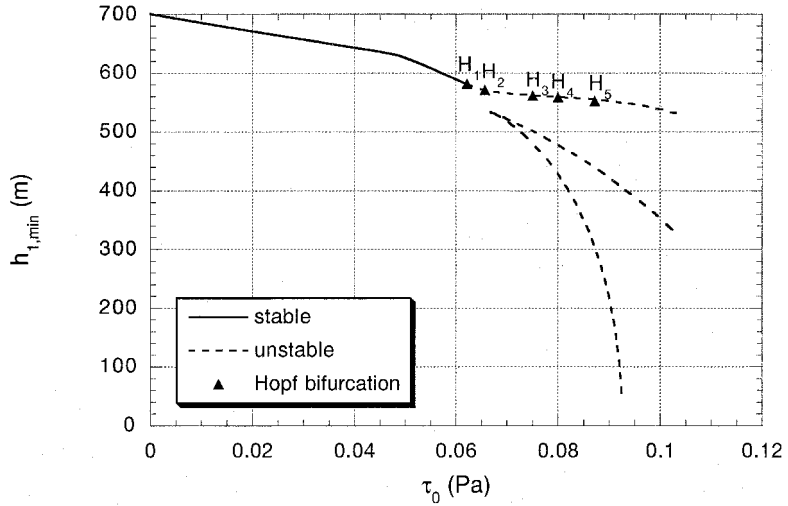

Figure 1. Bifurcation diagram of the two-layer shallow-water model. To monitor the solutions the minimum upper layer thickness $h_{1,\min}$ is plotted versus the wind stress strength τ_0. Drawn (dashed) lines indicate stable (unstable) steady states and the markers labeled $H_1, \ldots, H_5$ indicate Hopf bifurcations.

with angular frequency σ_i and growth rate σ_r. The dimensional period of oscillation $\mathcal{P}$ is given by $\mathcal{P} = 2\pi/\sigma_i$. The locations of the Hopf bifurcations $H_1, \ldots, H_5$ and the oscillation periods of each mode are presented in the second column of Table 2. The propagation of the mode can be followed by looking for example at $\mathbf{P}(-\pi/2\sigma_i) = \mathbf{P}(-\frac{1}{4}\mathcal{P}) = \mathbf{x}_I$ and then at $\mathbf{P}(0) = \mathbf{x}_R$.

To investigate whether the character of the mode is baroclinic or barotropic, a

Table 2. (a) Values of τ_0 (Pa) at which modes destabilize the steady states along the upper branch in Figure 1. (b) Oscillation periods of these modes at the Hopf bifurcations. Results are shown for the (standard) flat bottom case and for two different cases of bottom topography discussed in Section 3c.

Hopf bifurcation	τ_0 (flat)	τ_0 ('shelf')	τ_0 ('shelf + ridge')	
H_1	$6.2 \cdot 10^{-2}$	$6.6 \cdot 10^{-2}$	$7.2 \cdot 10^{-2}$	
H_2	$6.6 \cdot 10^{-2}$	$7.4 \cdot 10^{-2}$	$7.4 \cdot 10^{-2}$	
H_3	$7.4 \cdot 10^{-2}$	$7.8 \cdot 10^{-2}$	$7.8 \cdot 10^{-2}$	(a)
H_4	$8.0 \cdot 10^{-2}$	$8.5 \cdot 10^{-2}$		
H_5	$8.7 \cdot 10^{-2}$			

Hopf bifurcation	$\mathcal{P}$ (flat)	$\mathcal{P}$ ('shelf')	$\mathcal{P}$ ('shelf + ridge')	
H_1	4.8 mo	3.2 mo	2.7 mo	
H_2	2.8 mo	3.4 mo	3.1 mo	
H_3	5.6 mo	2.1 mo	26.1 yr	(b)
H_4	2.6 mo	5.3 yr		
H_5	12.7 yr			

pseudostreamfunction, ψ_i ($i = 1, 2$), will be plotted for both layers, defined by $u_i = -(\partial\psi_i/\partial y)$ and $v_i = (\partial\psi_i/\partial x)$. With this definition the flow is tangent to lines of constant ψ_i.

The upper layer streamfunction of the steady state, which becomes unstable at Hopf bifurcation H_1 at a wind stress strength of $\tau_0 = 6.2 \times 10^{-2}$ Pa, is shown in Figure 2a. At this wind stress strength, the flow already shows a strong jet and well-developed recirculation gyres. The imaginary and real parts of the eigenvector (both for the upper and lower layer) are plotted in Figures 2b–e. In both layers, the mode is localized in the jet and the propagation is eastward. If we compare the positions of the extrema in the upper layer streamfunction (Fig. 2c) with the ones in the lower layer streamfunction at a quarter of a period earlier (Fig. 2d), we see a phase difference of approximately $\frac{1}{4}\mathcal{P}$, which is characteristic of a baroclinic instability. If we could superpose these perturbations linearly on the steady state, we would obtain a meandering jet with an oscillation period of 4.8 months. This mode clearly can be identified with the first destabilized baroclinic mode of the two-layer quasi-geostrophic model (Dijkstra and Katsman (1997), their Fig. 9 or Dijkstra *et al.* (1999), their Figs. 21a, b).

The steady state and the real and imaginary parts of the mode at Hopf bifurcation H_2 ($\tau_0 = 6.6 \times 10^{-2}$ Pa) are plotted in Figure 3. At this value of τ_0, the mean state has hardly changed with respect to that in Figure 2a. The oscillatory mode has a basin-wide structure, resembling westward traveling Rossby basin modes, which interact with the recirculation gyres. The period of this mode ($\mathcal{P}_2 = 2.8$ mo) is indeed in the intermonthly range and its structure is fairly barotropic. The perturbations seem to be growing in the north (south) of the subpolar (subtropical) recirculation gyre, where the velocity of the steady state is in the same direction as the phase velocity of the perturbations. At the location of the jet, the perturbations of opposite sign would cause the strength of the jet to vary, while the recirculation gyres will show meandering when the perturbations are superposed on the steady state. This mode can be identified with the first barotropic Rossby basin mode, which also destabilizes in the 1.5-layer shallow-water model (Dijkstra and Molemaker (1999), their Figs. 6a, b); the latter is related to the first basin mode in the quasi-geostrophic model (Dijkstra and Katsman (1997), their Fig. 5).

The steady state and the patterns of the destabilizing mode at Hopf bifurcation H_3 ($\tau_0 = 7.4 \times 10^{-2}$ Pa) are shown in Figure 4. The oscillation period of this mode ($\mathcal{P}_3 = 5.6$ mo) is quite similar to that of the mode which destabilizes at Hopf bifurcation H_1. The spatial structure has a baroclinic character but its extent is broader and it is more aligned with the steady state jet. As a next baroclinic mode, one would have expected the antisymmetric baroclinic mode of the 2-layer quasi-geostrophic model as in Dijkstra and Katsman (1997) (their Fig. 10), but this mode clearly looks more like the third symmetric baroclinic mode, presented in Dijkstra *et al.* (1999) (their Figs. 21e, f). The asymmetry of the steady-state jet apparently gives a preference for modes, which are symmetric with respect to the jet axis, but the reason for this preference is not easily explained. The mode arising at Hopf bifurcation H_4 ($\tau_0 = 8.0 \times 10^{-2}$ Pa) resembles the mode at Hopf bifurcation H_2 (Fig. 5)

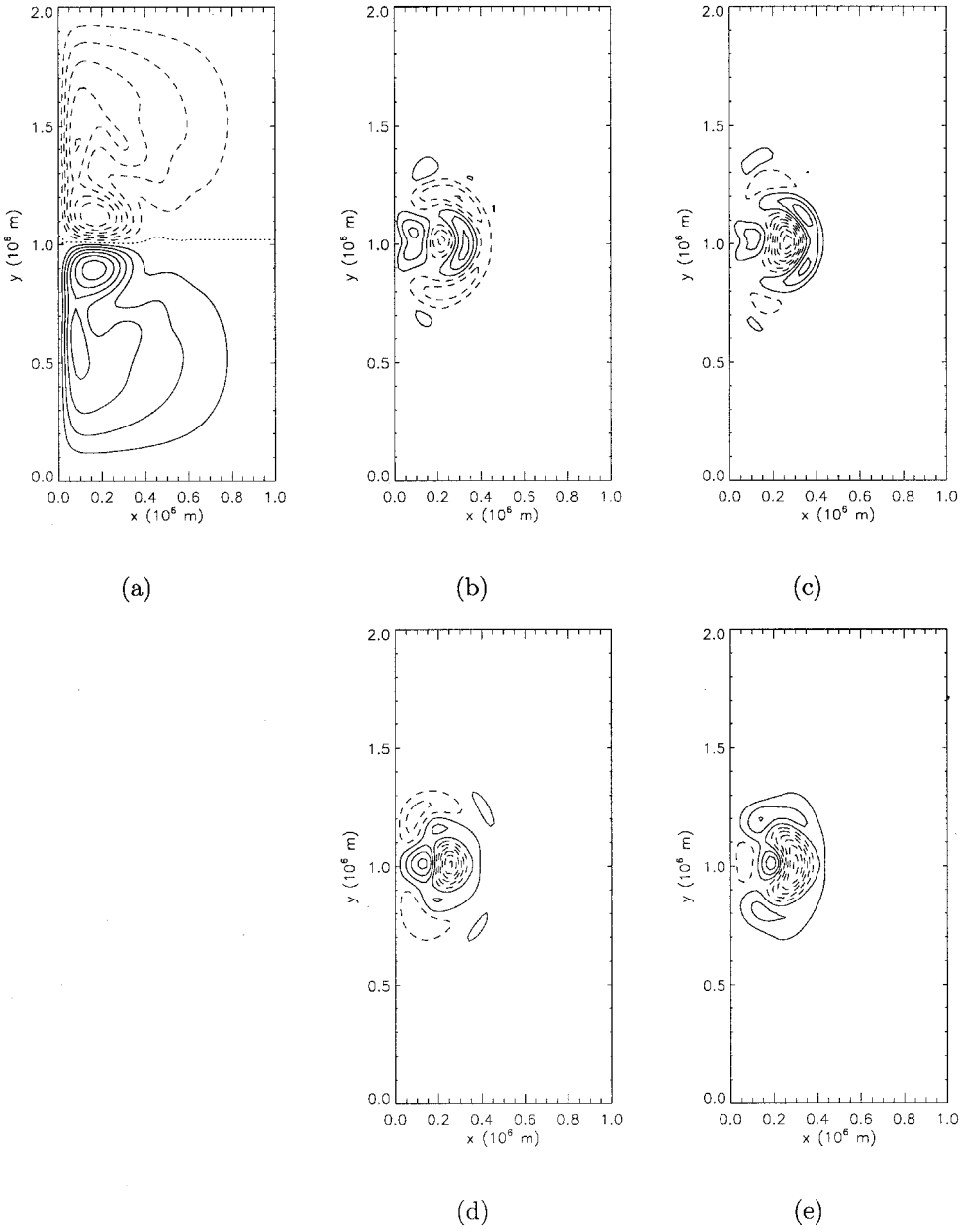

Figure 2. Panel (a) shows the upper layer streamfunction of the steady state at Hopf bifurcation H_1 at a wind stress of $\tau_0 = 6.2 \times 10^{-2}$ Pa. Panels (b) and (c) show the imaginary and real parts of the perturbation of the upper layer streamfunction and panels (d) and (e) of the lower layer streamfunction. The mode has a period of $\mathcal{P}_1 = 4.8$ mo.

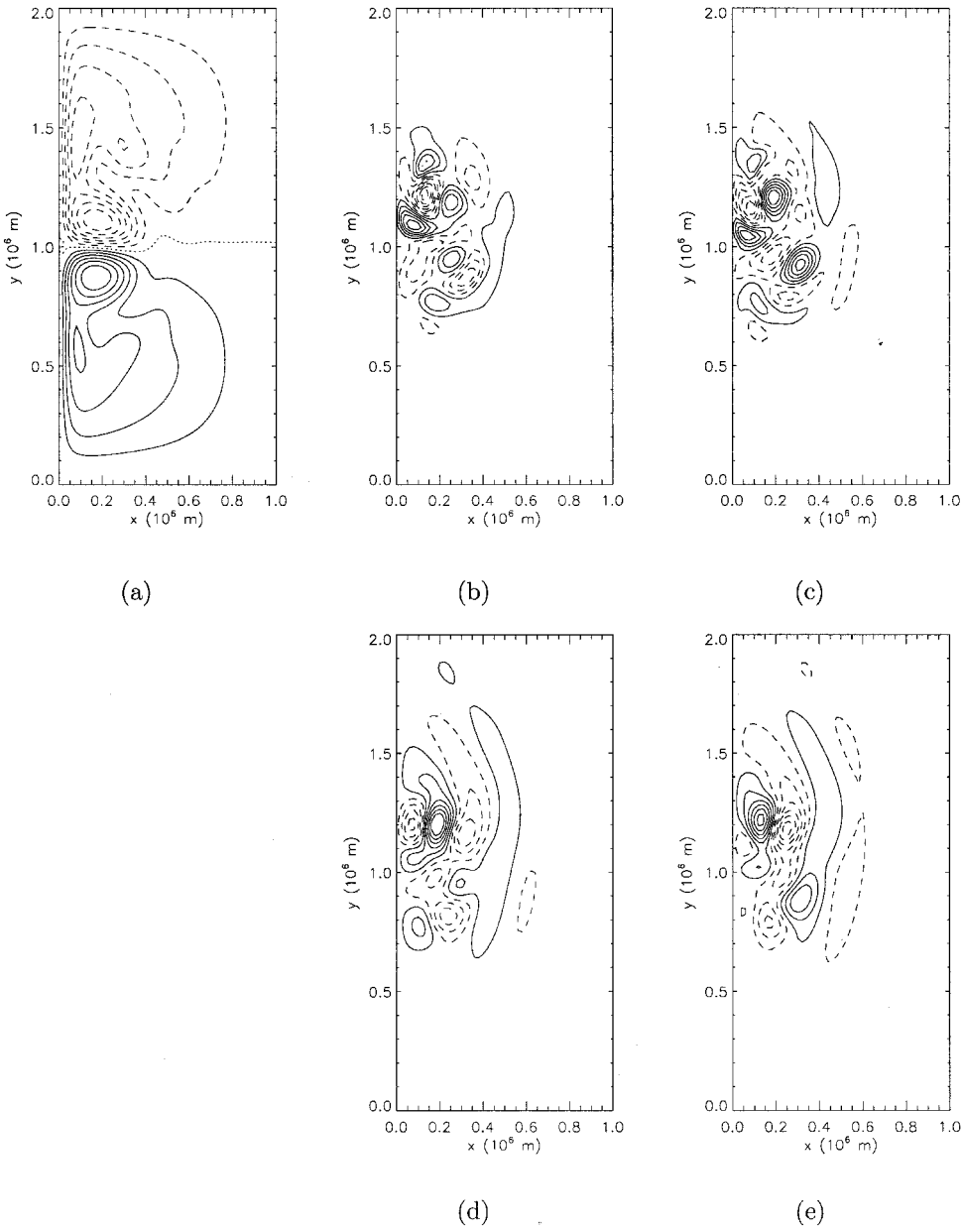

Figure 3. Panel (a) shows the upper layer streamfunction of the steady state at Hopf bifurcation H_2 at a wind stress of $\tau_0 = 6.6 \times 10^{-2}$ Pa. Panels (b) and (c) show the imaginary and real parts of the perturbation of the upper layer streamfunction and panels (d) and (e) of the lower layer streamfunction. The mode has a period of $\mathcal{P}_2 = 2.8$ mo.

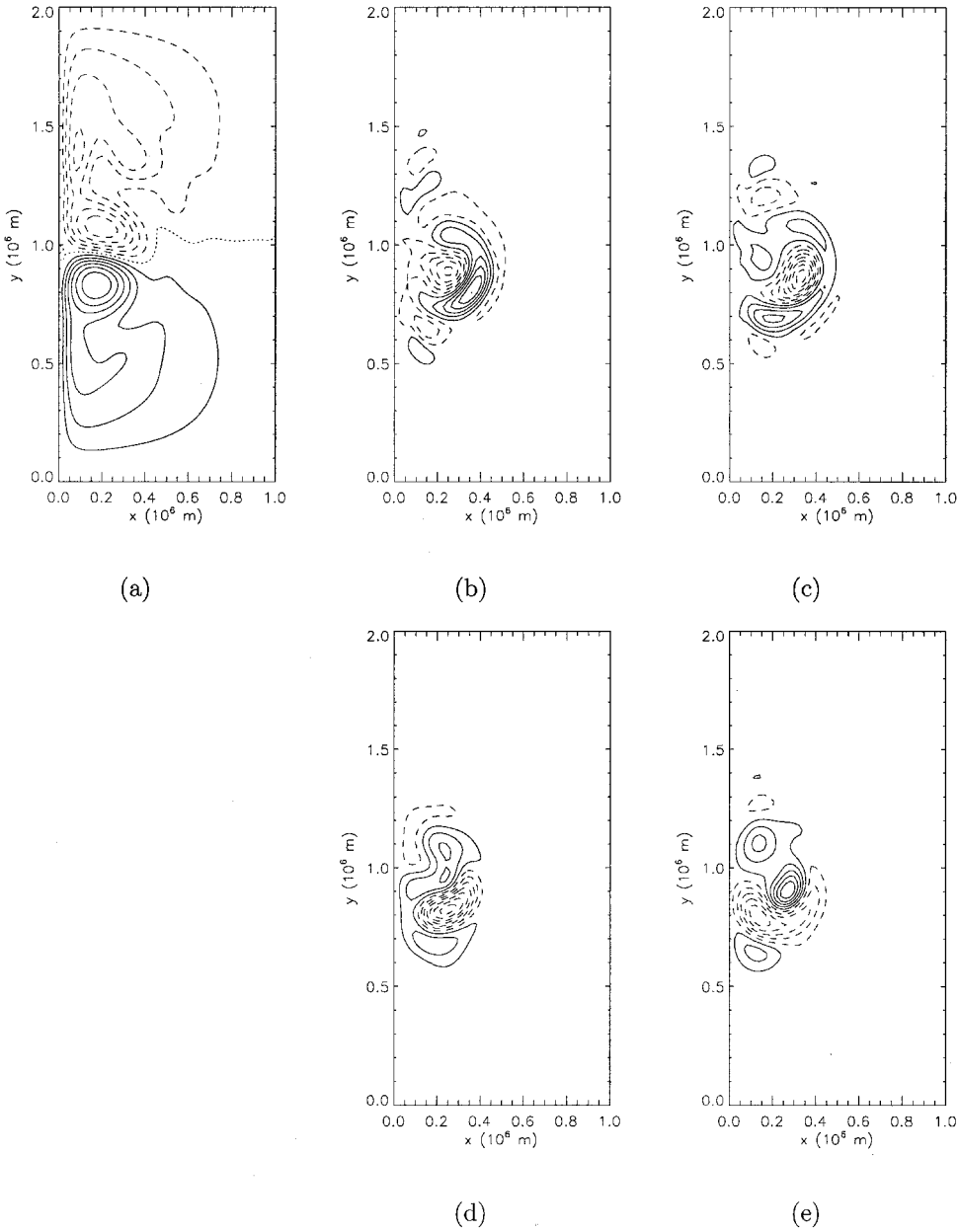

Figure 4. Panel (a) shows the upper layer streamfunction of the steady state at Hopf bifurcation H_3 at a wind stress of $\tau_0 = 7.4 \times 10^{-2}$ Pa. Panels (b) and (c) show the imaginary and real parts of the perturbation of the upper layer streamfunction and panels (d) and (e) of the lower layer streamfunction. The mode has a period of $\mathcal{P}_3 = 5.6$ mo.

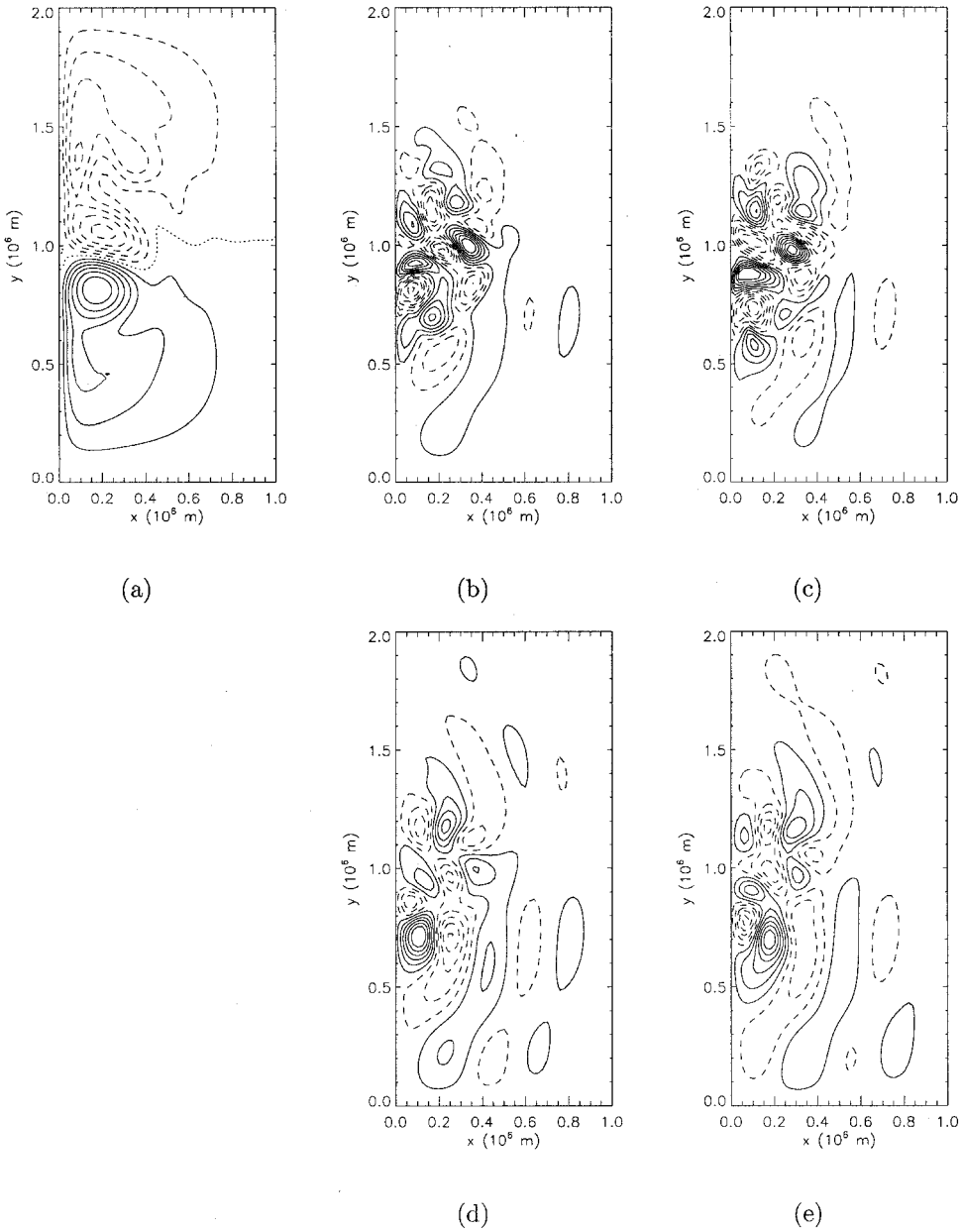

Figure 5. Panel (a) shows the upper layer streamfunction of the steady state at Hopf bifurcation H_4 at a wind stress of $\tau_0 = 8.0 \times 10^{-2}$ Pa. Panels (b) and (c) show the imaginary and real parts of the perturbation of the upper layer streamfunction and panels (d) and (e) of the lower layer streamfunction. The mode has a period of $\mathcal{P}_4 = 2.6$ mo.

and one of the intermonthly modes in the 1.5-layer model (Dijkstra and Molemaker, 1999). Again, the extent of this mode is basin wide and its period is short ($\mathcal{P}_4 = 2.6$ mo), which indicates that this is another destabilized Rossby basin mode.

The steady-state streamfunction at a wind stress strength of $\tau_0 = 8.7 \times 10^{-2}$ Pa and the imaginary and real parts of the streamfunction of the mode, which destabilizes at H_5 are shown in Figure 6. This mode has an oscillation period of 12.7 yr, which is in the low-frequency range. The spatial pattern of the mode displays a strong alignment with the direction of the jet; its extrema are located along a line through the extrema in the steady-state streamfunction of the subtropical and subpolar gyre. It can be seen from Figures 6b–d that this mode has a baroclinic character. The flow imagined of this perturbation superposed on the steady state is one in which the jet is strengthened and weakened. A barotropic equivalent of this mode, called a 'gyre' mode with a shorter (interannual) time scale, has been found in 1.5-layer shallow-water models (Speich *et al.* (1995), their Fig. 7) and in quasi-geostrophic barotropic models (Dijkstra and Katsman (1997), their Fig. 6). The sequence of Hopf bifurcations on the upper branch nicely shows that the classical baroclinic modes and the barotropic Rossby basin modes destabilize alternately and that eventually a low-frequency baroclinic 'gyre' mode destabilizes.

b. Transient flows: Flat bottom case

Having the structure and frequencies of the first modes which destabilize the steady states at the upper branch, next transient flows are computed by integrating the governing equations forward in time. As an initial condition, the state of rest or one of the steady states found with the continuation method is taken. Time-dependent flows have been calculated for several distinct values of the wind stress parameter τ_0 and as an indicator of the character of the flow, we now use the (5-year) time-averaged minimum upper layer thickness, $\bar{h}_{1,\min}$. In Figure 7, the bifurcation diagram together with the minimum upper layer thickness of the transient flows are plotted; the marker shows its average and the 'error' bar its range over time.

For the values up to $\tau_0 = 6.0 \times 10^{-2}$ Pa, a steady double-gyre flow in the upper layer is found with a motionless lower layer. The correspondence of the values of $h_{1,\min}$ for both the transient flow code and the continuation code (which are totally different) is reassuring that both codes obtain similar solutions. The time series of the basin integrated kinetic energy, $\mathcal{E}_k$, defined as

$$\mathcal{E}_k = \sum_{i=1}^{2} \frac{\rho_i}{2} \int h_i(u_i^2 + v_i^2)\, dxdy \tag{9}$$

is plotted at $\tau_0 = 6.3 \times 10^{-2}$ Pa in Figure 8a. A high-frequency periodic orbit is found and the Fourier spectrum of this time series (Fig. 8b) has a broad peak centered around a period $\mathcal{P} = 4.74$ mo and a very small peak near its first harmonic, at $\mathcal{P} = 2.34$ mo. The period of

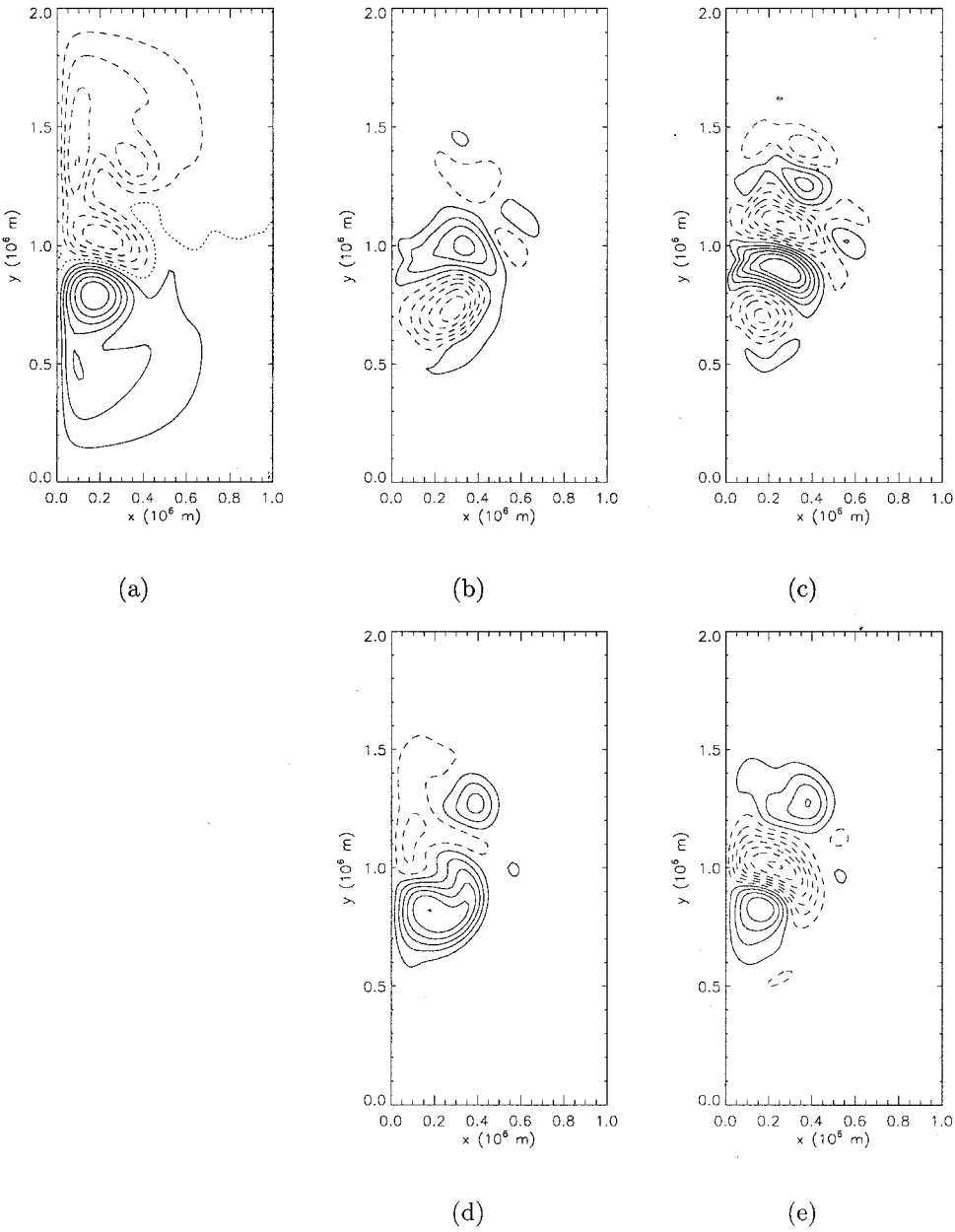

Figure 6. Panel (a) shows the upper layer streamfunction of the steady state at Hopf bifurcation H_5 at a wind stress of $\tau_0 = 8.7 \times 10^{-2}$ Pa. Panels (b) and (c) show the imaginary and real parts of the perturbation of the upper layer streamfunction and panels (d) and (e) of the lower layer streamfunction. The mode has a period of $\mathcal{P}_5 = 12.7$ yr.

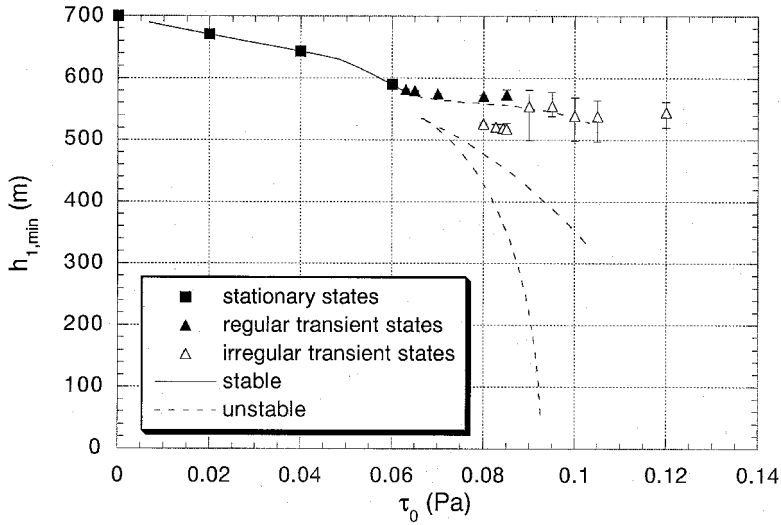

Figure 7. Bifurcation diagram showing the minimum upper layer thickness $h_{1,min}$ versus the strength of the wind stress τ_0 for the steady states (as in Fig. 1). The markers indicate the average minimum upper layer thickness $\bar{h}_{1,min}$ of the computed time-dependent solutions and the bars indicate their range.

this orbit is indeed similar to the period at Hopf bifurcation H_1 ($\mathcal{P}_1 = 4.79$ mo) because the forcing ($\tau_0 = 6.3 \times 10^{-2}$ Pa) is only slightly supercritical.

The time series of the basin integrated kinetic energy for $\tau_0 = 7.0 \times 10^{-2}$ Pa (Fig. 8c) consists of two frequencies. This is confirmed by the spectrum of this time series (Fig. 8d), showing two broad peaks centered around $\mathcal{P} = 4.0$ mo and around $\mathcal{P} = 1.94$ mo. This signal consists of two oscillations, which originate through the instabilities at Hopf bifurcations H_1 and H_2, (τ_0, $\mathcal{P}_1$) = (6.2×10^{-2} Pa, 4.8 mo) and (τ_0, $\mathcal{P}_2$) = (6.6×10^{-2} Pa, 2.8 mo). The second peak is higher than the first, because it possibly also contains the first harmonic of the first peak.

Within the small interval $8.0 \times 10^{-2} < \tau_0 < 8.5 \times 10^{-2}$ Pa, two different time-dependent solutions are found when starting from different initial conditions. A solution with a value for $\bar{h}_{1,min}$ around 570 m is obtained when the transient flow computation is initialized with a steady state solution of the upper branch or with the state of rest. The solution characterized by a value of $\bar{h}_{1,min}$ around 520 m is obtained by initializing with a steady state solution of the isolated branch. The last five years of the time series of $h_{1,min}$ are shown in Figure 9a for both trajectories at $\tau_0 = 8.0 \times 10^{-2}$ Pa. The time series of the upper branch solution still seem quite periodic, while the time series of the lower branch already shows variability on several different time scales. The 5-year averaged upper layer thickness of the solution with $\bar{h}_{1,min} = 572$ m is plotted in Figure 9b and shows a western boundary current, which deflects southward after separation. The 5-year averaged solution with $\bar{h}_{1,min} = 526$ m in Figure 9c, displays a northward deflected current.

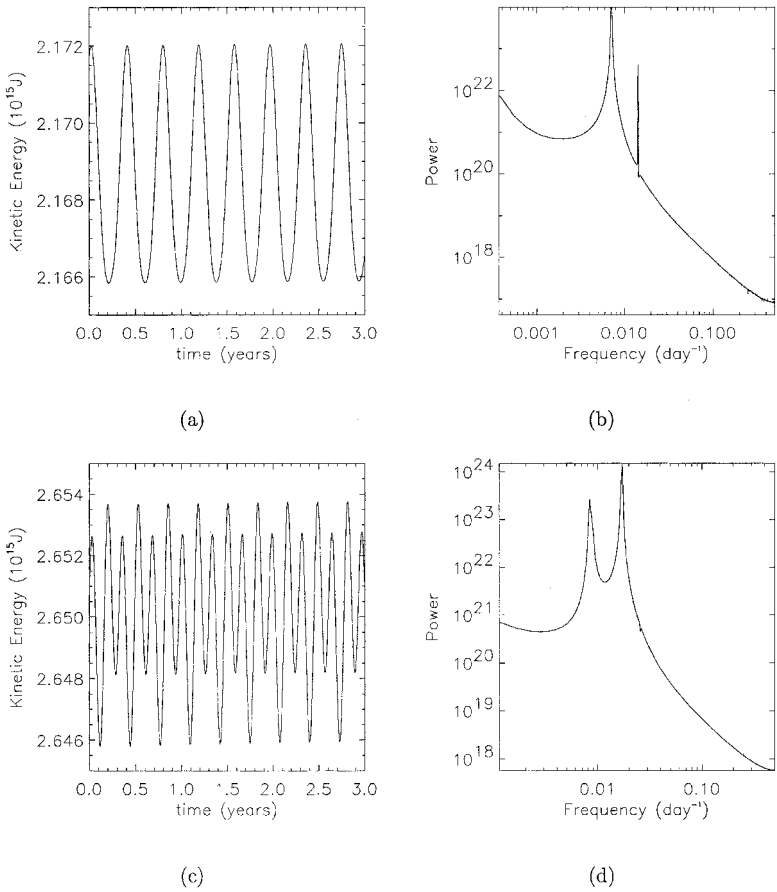

Figure 8. (a) Time series of the basin integrated kinetic energy at a wind stress of (a) $\tau_0 = 6.3 \times 10^{-2}$ Pa and (c) $\tau_0 = 7.0 \times 10^{-2}$ Pa; (b) and (d) show the Fourier power spectra of (a) and (c), respectively.

At values of $\tau_0 > 8.5 \times 10^{-2}$ Pa, no multiple time-dependent flows are found anymore. The time series of the basin-integrated kinetic energy at $\tau_0 = 8.5 \times 10^{-2}$ Pa of the one with $\bar{h}_{1,\min} = 570$ m (Fig. 10a) displays a low-frequency oscillation with a period of 18 yr together with high-frequency oscillations. At a higher wind stress forcing of $\tau_0 = 1.05 \times 10^{-1}$ Pa the time series of the basin integrated kinetic energy shows irregular behavior (Fig. 10b) with large fluctuations in the kinetic energy on intervals of approximately 10 yr. In order to find the pattern of variability which is associated with the low-frequency oscillations at these values of the wind stress strength, the streamfunctions of both layers, ψ_i, as defined in Section 3a, are sampled each month over a 60-year period. The number of degrees of freedom is reduced by performing a standard Principal Component Analysis (PCA). The resulting 10 leading Principal Components (PCs), which account for 99.9% of

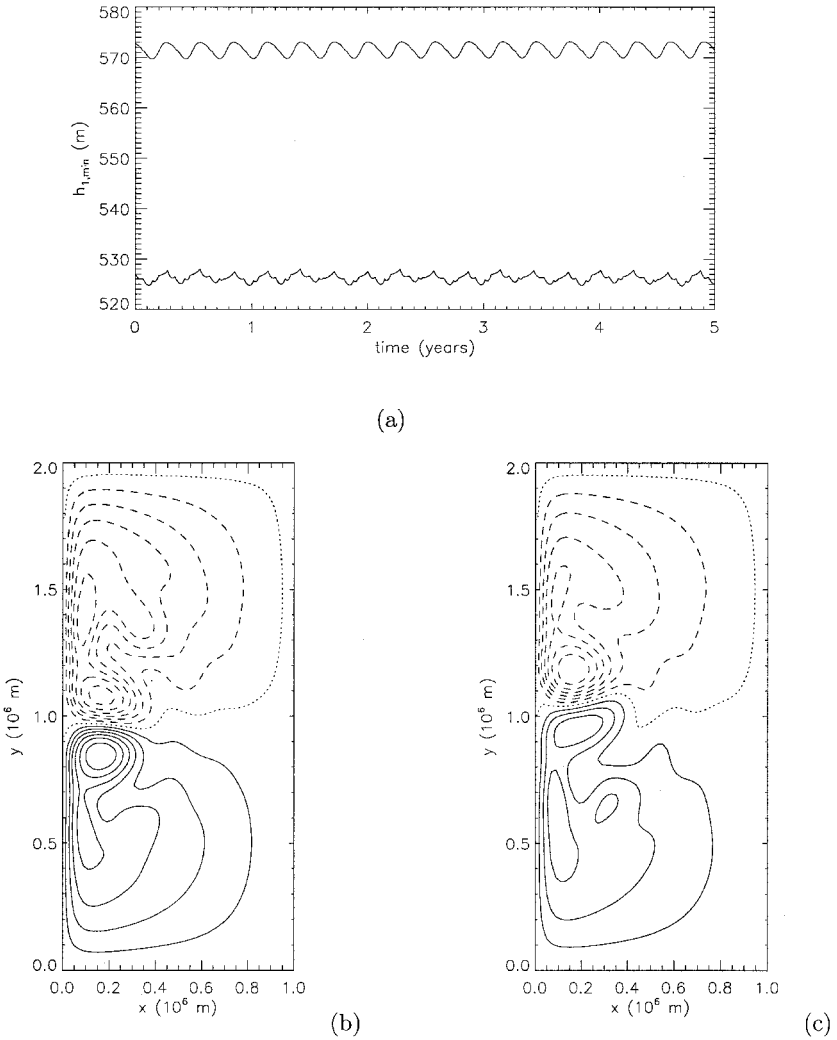

Figure 9. (a) The last five years of the time series of the minimum upper layer thickness, $h_{1,\min}$, for the two time-dependent solutions at a wind stress of $\tau_0 = 8.0 \times 10^{-2}$ Pa. Five-year averages of the upper layer thickness of the upper time series in (b) and the lower time series in (c).

the variance at $\tau_0 = 8.5 \times 10^{-2}$ Pa and 92% at $\tau_0 = 1.05 \times 10^{-1}$ Pa, are the input for a Multichannel Singular Spectrum Analysis (MSSA) (Plaut and Vautard, 1994). A window length of $M = 20$ yr and $M = 15$ yr is taken at $\tau_0 = 8.5 \times 10^{-2}$ Pa and $\tau_0 = 1.05 \times 10^{-1}$ Pa, respectively. From the MSSA analysis, a low-frequency statistical mode is found with an oscillation period $\mathcal{P} = 18$ yr at $\tau_0 = 8.5 \times 10^{-2}$ Pa which explains 22% of the total variance within the 20-year window. Snapshots of the upper and lower layer streamfunction of the reconstructed components are shown in Figure 11. The fields are plotted at

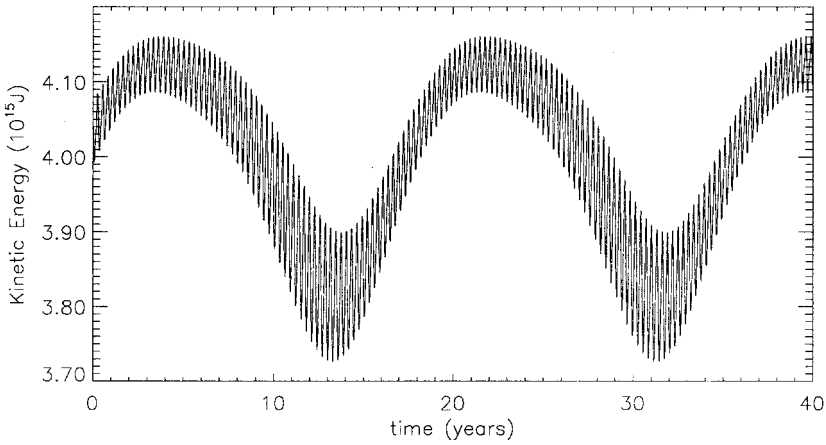

(a)

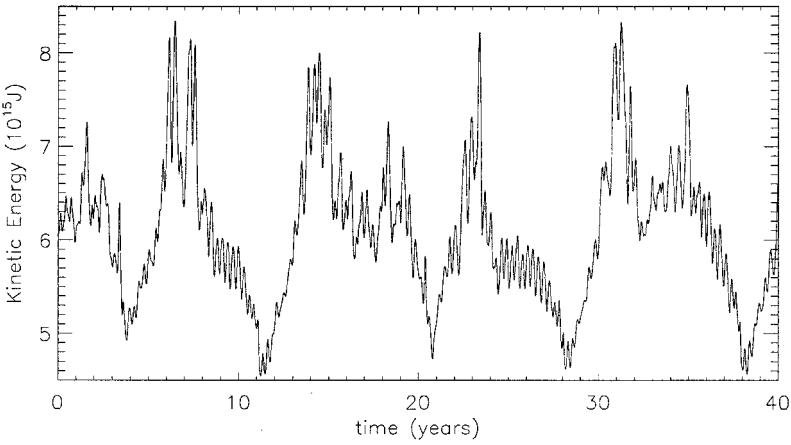

(b)

Figure 10. Time series of the basin integrated kinetic energy at a wind stress of $\tau_0 = 8.5 \times 10^{-2}$ Pa in panel (a) and $\tau_0 = 1.05 \times 10^{-1}$ Pa in (b).

approximately the same stages of the oscillation as the low-frequency mode destabilizing at H_5 (Fig. 6). Note that the latter mode is still linearly stable at this wind stress strength (see Table 2a). There is a good correspondence between the upper layer streamfunctions of the low-frequency mode and of the time-dependent variations of the statistical mode. However, the vertical structure of the low-frequency mode is clearly baroclinic, while the time variation of the statistical mode is a mix of a baroclinic phase (i.e., at $t = 0$, Figs. 11a,

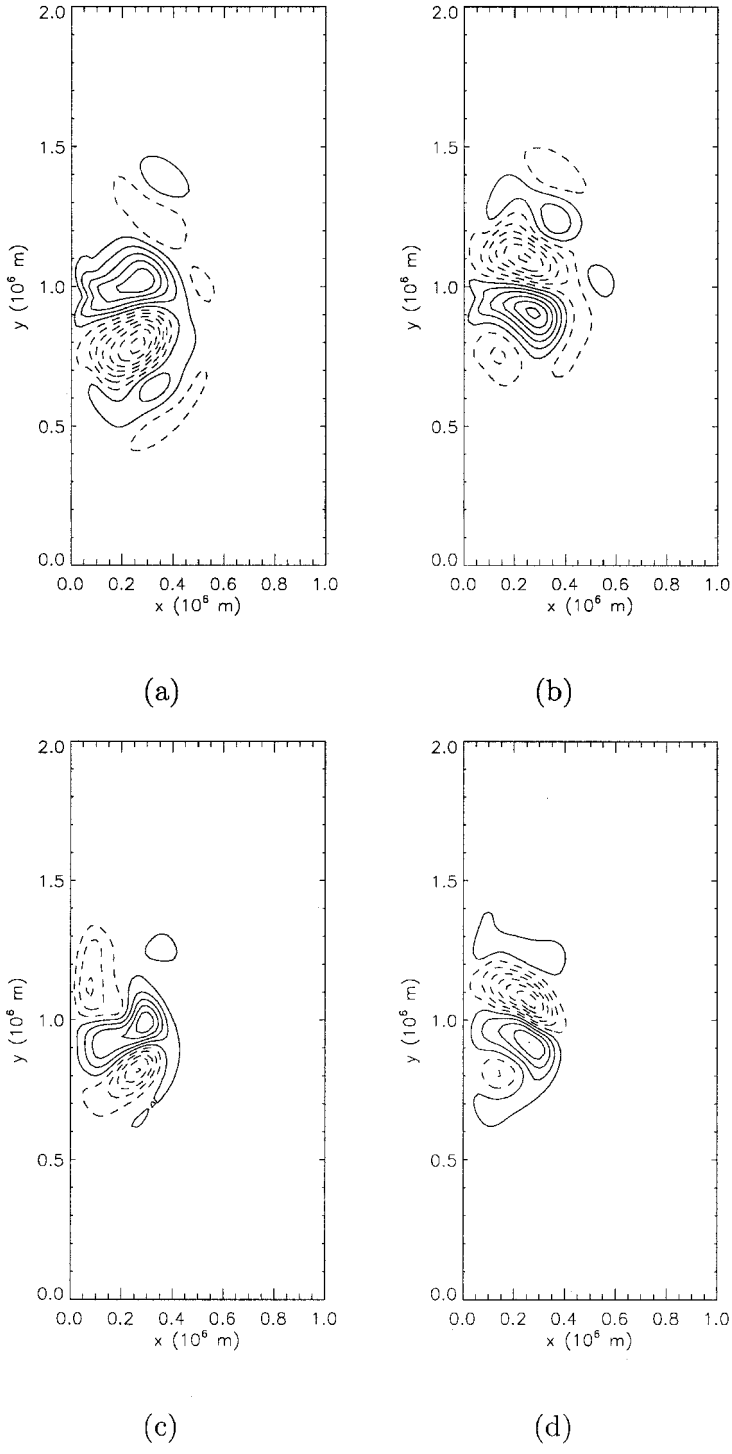

Figure 11. Reconstructed component of the low-frequency statistical mode obtained through MSSA analysis. Upper layer streamfunction at $\tau_0 = 8.5 \times 10^{-2}$ Pa at $t = 0$ in panel (a) and at $t = 4.5$ yr in panel (b) and the lower layer streamfunction in (c) and (d). The period of this oscillation is $\mathcal{P} = 18$ yr and it explains 22% of the variance within the 20-year window.

c) and a more barotropic phase (i.e., at $t = 4.5$ yr, Figs. 11b, d). Even with these differences in the lower layer response, the correspondence between the upper layer patterns supports the notion that the dominant low-frequency time variations in the transient flow can be attributed to the presence of the low-frequency mode, which destabilizes the steady state at Hopf bifurcation H_5. A similar dominant low-frequency statistical mode is found from the transient flow at $\tau = 1.05 \times 10^{-1}$ Pa, having a period of $\mathcal{P} = 8.0$ yr and explaining 54% of the variance within the 15-year window. Snapshots of the upper and lower layer streamfunction of this statistical mode are shown in Figure 12. The reconstructed component now shows an even more barotropic signal, which explains its decrease in oscillation period. The shape of the anomalies in the upper layer still show much resemblance with the mode which is destabilized at Hopf bifurcation H_5. Hence, there seems to be a tendency toward barotropic modification of the 'gyre' mode with increasing τ_0.

The correspondence between the pattern of low-frequency variability in the transient flow and the 'gyre' mode is motivation to investigate the instantaneous flows for which the time series are plotted in Figure 10. Both time series indicate different levels of total kinetic energy associated with the low-frequency behavior. In Figure 13, two instantaneous streamfunctions are plotted for the case $\tau_0 = 1.05 \times 10^{-1}$ Pa at $t = 9$ yr (at which the transient flow has high kinetic energy) and at $t = 15$ yr (at which the transient flow has low kinetic energy). In the high-energy state (Figs. 13a/c), the zonal jet is strong and meandering is weak. In the low-energy state (Figs. 13b/d), meandering is very strong and a 'ring' is present. Both states have similar characteristics as the high- and low-energy states found in quasi-geostrophic models (McCalpin and Haidvogel, 1996; Berloff and McWilliams, 1999). Coupling these characteristics with the earlier correspondence of the low-frequency behavior strongly suggests that the appearance of low-frequency variability in the form of high- and low-energy states can be attributed to the destabilization of the baroclinic 'gyre' mode.

c. Sensitivity to bottom topography

In this section, we aim to demonstrate that the low-frequency mode is not solely characteristic for the flat bottom case. The nice element of the two-layer set-up is that even with bottom topography, the steady-state structure is still the same as for the flat bottom case, since the lower layer is motionless. Hence, only the instabilities, i.e., the position and patterns of the Hopf bifurcations are modified. Two shapes of the bottom topography are considered: one of these mimics a continental shelf with the following simple shape of the bottom topography,

$$H_b(x, y) = \begin{cases} \dfrac{h_b}{2}\left[1 + \cos\left(\dfrac{2\pi x}{\lambda_0}\right)\right] & 0 < x < \dfrac{1}{2}\lambda_0 \\ 0.0 & \text{otherwise} \end{cases} \tag{10}$$

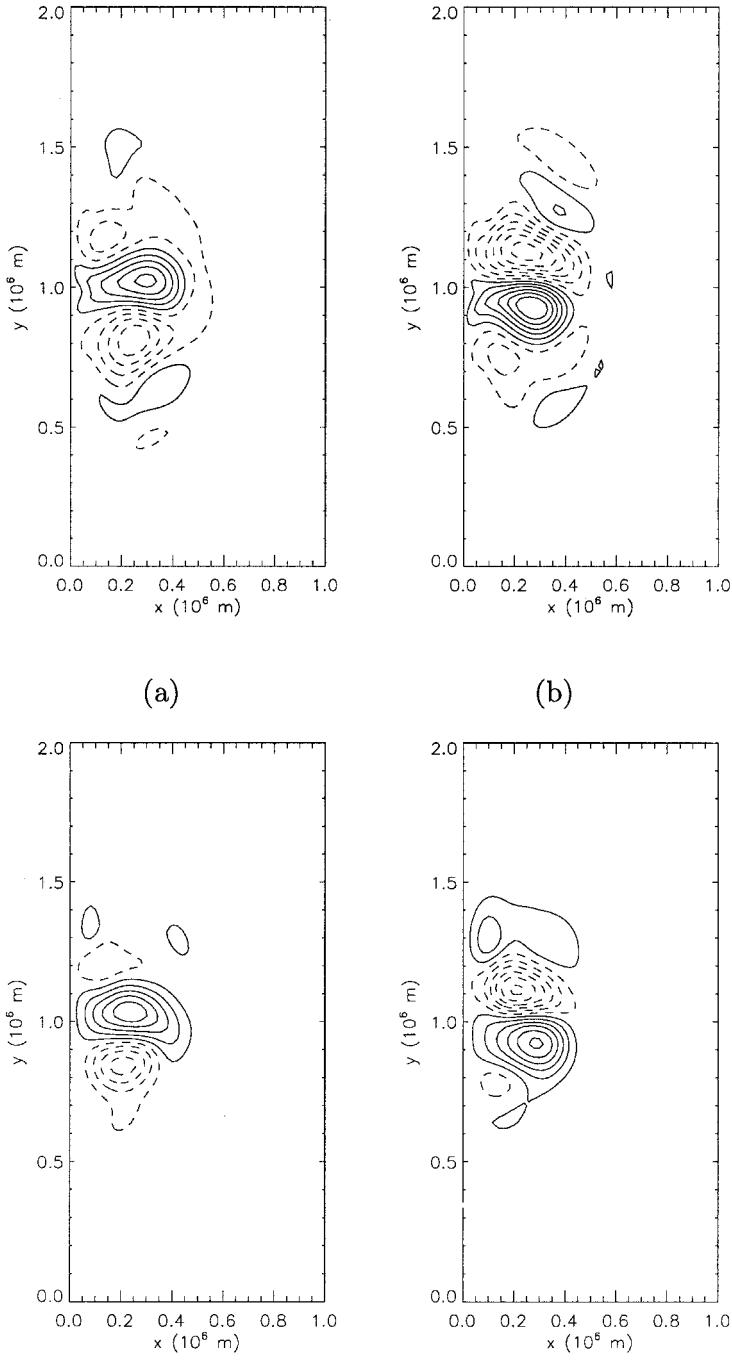

Figure 12. Reconstructed component of the low-frequency statistical mode obtained through MSSA analysis. Upper layer streamfunction at $\tau_0 = 1.05 \times 10^{-1}$ Pa at $t = 7.5$ yr in panel (a) and at $t = 9.5$ yr in panel (b) and the lower layer streamfunction in (c) and (d). The period of this oscillation is $\mathcal{P} = 8.0$ yr and it explains 54% of the variance within the 15-year window.

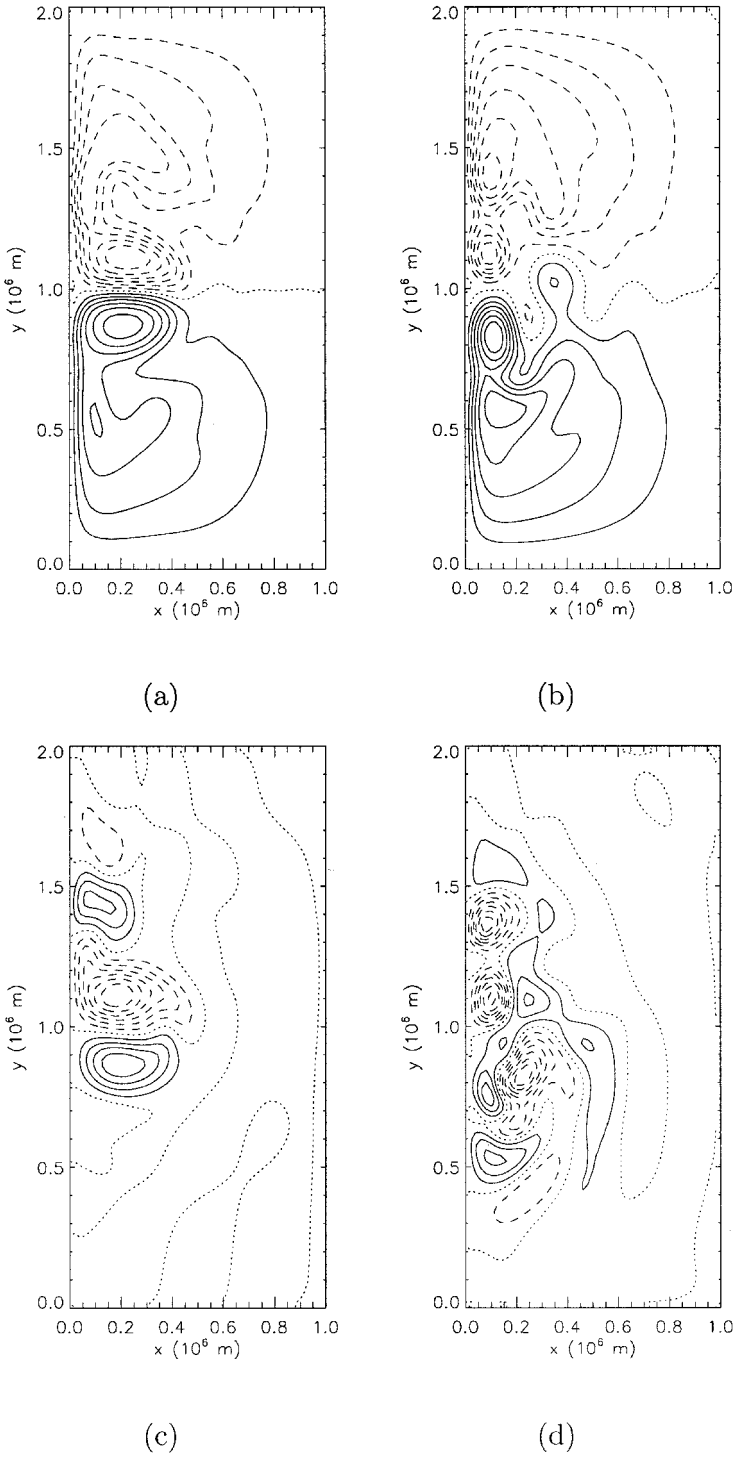

Figure 13. In panels (a) and (c) are snapshots of the streamfunctions of the upper and lower layer during the high-energy period at $t = 9$ yr; (b) and (d) during the low-energy period at $t = 15$ yr at $\tau_0 = 1.05 \times 10^{-1}$ Pa.

where $h_b = 100$ m is the maximum height of the shelf and $\lambda_0 = 600$ km is its wavelength. The effect of a continental shelf in combination with a mid-basin ridge is represented using the following shape of the bottom topography

$$H_b(x, y) = \begin{cases} \dfrac{h_b}{6}\left[1 + \cos\left(\dfrac{2\pi x}{\lambda_0}\right)\right] & 0 < x < \dfrac{1}{2}\lambda_0 \\ \dfrac{h_b}{2}\left[1 + \cos\left(\dfrac{2\pi x}{\lambda_0}\right)\right] & \dfrac{1}{2}\lambda_0 < x < \dfrac{3}{2}\lambda_0 \\ 0.0 & \text{otherwise} \end{cases} \tag{11}$$

here $h_b = 300$ m and $\lambda_0 = 400$ km. The height of both types of bottom topography has been chosen rather small compared to the total depth to compensate for the much larger effect of bottom topography on a two-layer flow than in a flow with realistic stratification.

The values of τ_0 and the oscillation periods of the destabilizing modes associated with the Hopf bifurcations of the case with the 'shelf' topography can be found in the third column of Table 2. The position of the first baroclinic Hopf bifurcation, H_1, is moved from $\tau_0 = 6.2 \times 10^{-2}$ Pa toward a slightly higher value of $\tau_0 = 6.6 \times 10^{-2}$ Pa, which indicates that this type of bottom topography increases the stability. The patterns of the modes, which destabilize the steady state at the first and second Hopf bifurcation, H_1 and H_2, are similar to the first and third Hopf bifurcations in the flat bottom case (on the basis of their pattern), but are now propagating in a northwest to southeast direction instead of in the west-east direction, as in the standard case. The third Hopf bifurcation H_3 is similar to the second (and fourth) Hopf bifurcation of the flat bottom case. The basin mode structure has become more pronounced, so that only the perturbations in the subtropical recirculation gyre are visible, while those in the subpolar recirculation gyre seem absent (not shown).

The low-frequency mode, which is now the fourth Hopf bifurcation H_4, has moved toward a smaller value of the wind stress forcing, from $\tau_0 = 8.7 \times 10^{-2}$ Pa in the flat bottom case toward $\tau_0 = 8.5 \times 10^{-2}$ Pa in the case with a 'shelf' topography. The spatial pattern of the mode (Fig. 14) has not changed dramatically compared to the flat bottom case (Fig. 6), although some effect of the bottom topography is visible in the lower layer pattern. However, the oscillation period has changed substantially from $\mathcal{P} = 12.7$ yr to $\mathcal{P} = 5.3$ yr. The perturbations in the lower layer of the flat bottom case are growing under the subpolar gyre and follow the flow of the subtropical recirculation gyre. With the 'shelf' topography, the perturbations are moving more southwestward in a direction along the contours of $f/\bar{h}_2$ south and southeast of the subtropical recirculation gyre. These contours are slightly more tilted in a northeast/southwest fashion compared to the flat bottom case as can be seen by comparing Figure 15a (flat bottom case) and Figure 15b ('shelf case').

For the 'shelf + ridge' topography, the τ_0 locations of the Hopf bifurcations and the oscillation periods of the modes can be found in the fourth column of Table 2. The

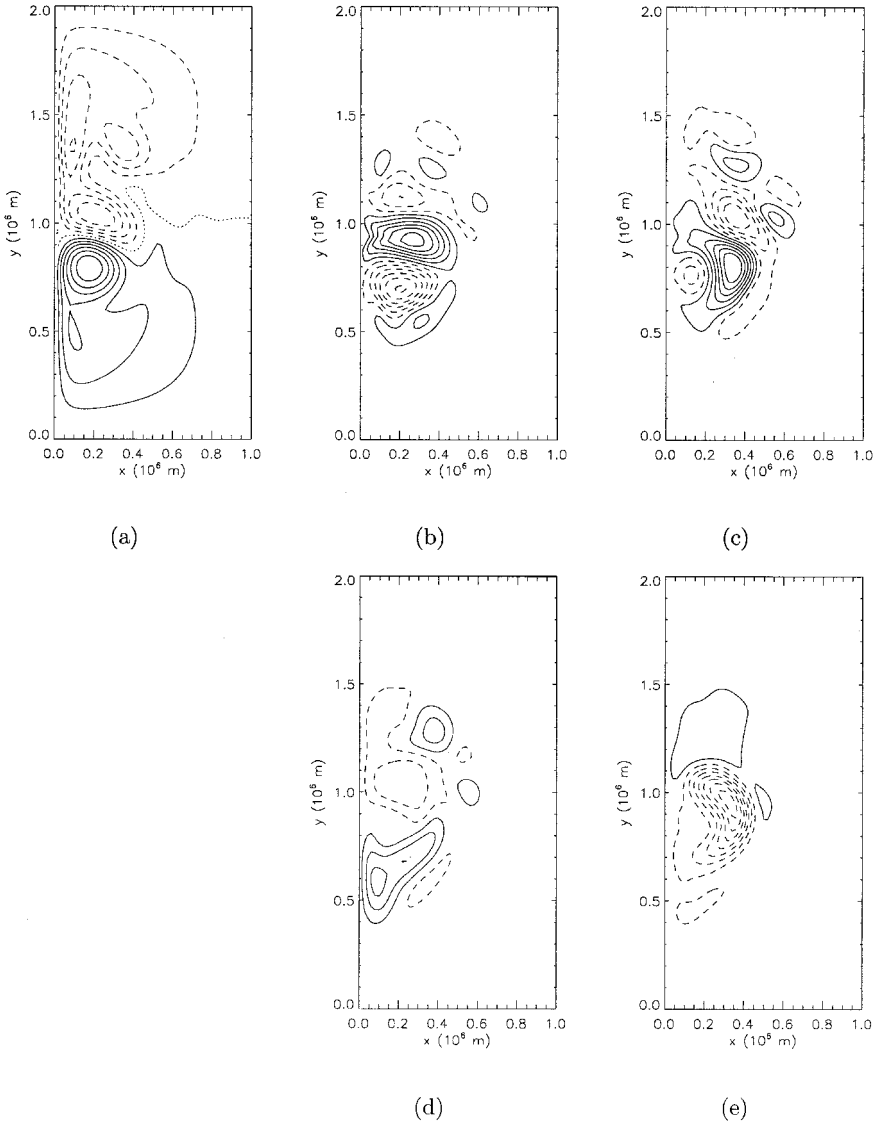

Figure 14. Panel (a) shows the upper layer streamfunction of the steady state at Hopf bifurcation H_4 in the case with the 'shelf' bottom topography of (10) at a wind stress of $\tau_0 = 8.5 \times 10^{-2}$ Pa. Panels (b) and (c) show the imaginary and real parts of the perturbation of the upper layer streamfunction and panels (d) and (e) of the lower layer streamfunction. The mode has a period of $\mathcal{P} = 5.3$ yr.

low-frequency mode now appears as the third Hopf bifurcation H_3; its period is 26 yr and its pattern is shown in Figure 16. The upper layer pattern is hardly modified by the bottom topography and can be quite easily related to the pattern at the fifth Hopf bifurcation of the

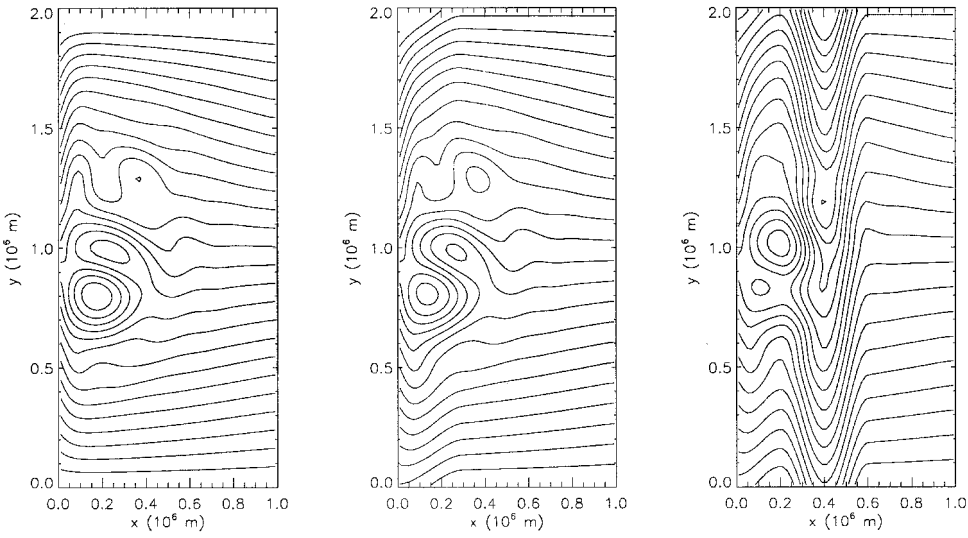

Figure 15. Contours of $f/\bar{h}_2$ are plotted at the Hopf bifurcation associated with low-frequency mode in (a) the flat bottom case, in (b) with the 'shelf' topography of (10) and in (c) with the 'shelf + ridge' topography of (11).

flat bottom case (Fig. 6). The lower layer perturbation flow is now strongly modified by the presence of the bottom topography. The dipole structure of the contours of $f/\bar{h}_2$ of more or less equal strength in the flat bottom case (Fig. 15a) has now almost changed into a monopole structure (Fig. 15c). The subtropical maximum, around which the patches of vorticity were transported in the previous two cases, has almost disappeared, which constrains the perturbations in the area below the subpolar gyre. However, what is most important is the shift of the Hopf bifurcation to much lower wind stress forcing, from $\tau_0 = 8.7 \times 10^{-2}$ Pa toward $\tau_0 = 7.8 \times 10^{-2}$ Pa. Hence, this type of bottom topography is able to destabilize the flow to a low-frequency mode at much lower wind stress forcing, without changing the upper-layer perturbation flow much. Again, this type of mode has the characteristics of weakening and strengthening the jet, when superposed on the steady state, and can, therefore, cause the low-frequency alternations between high- and low-energy states in the time-dependent flow.

The impact of this destabilization of the low-frequency mode with the 'shelf + ridge' bottom topography (11) is now subsequently tested through transient flow computations again initiated with a steady state solution. For $\tau_0 = 8.0 \times 10^{-2}$ Pa, the time series of the upper layer thickness indeed shows low-frequency behavior with an oscillation period of about $\mathcal{P} = 11$ yr (Fig. 17). The patterns of the statistical mode of low-frequency oscillation have been analyzed with MSSA and the reconstructed pair, which explained most of the

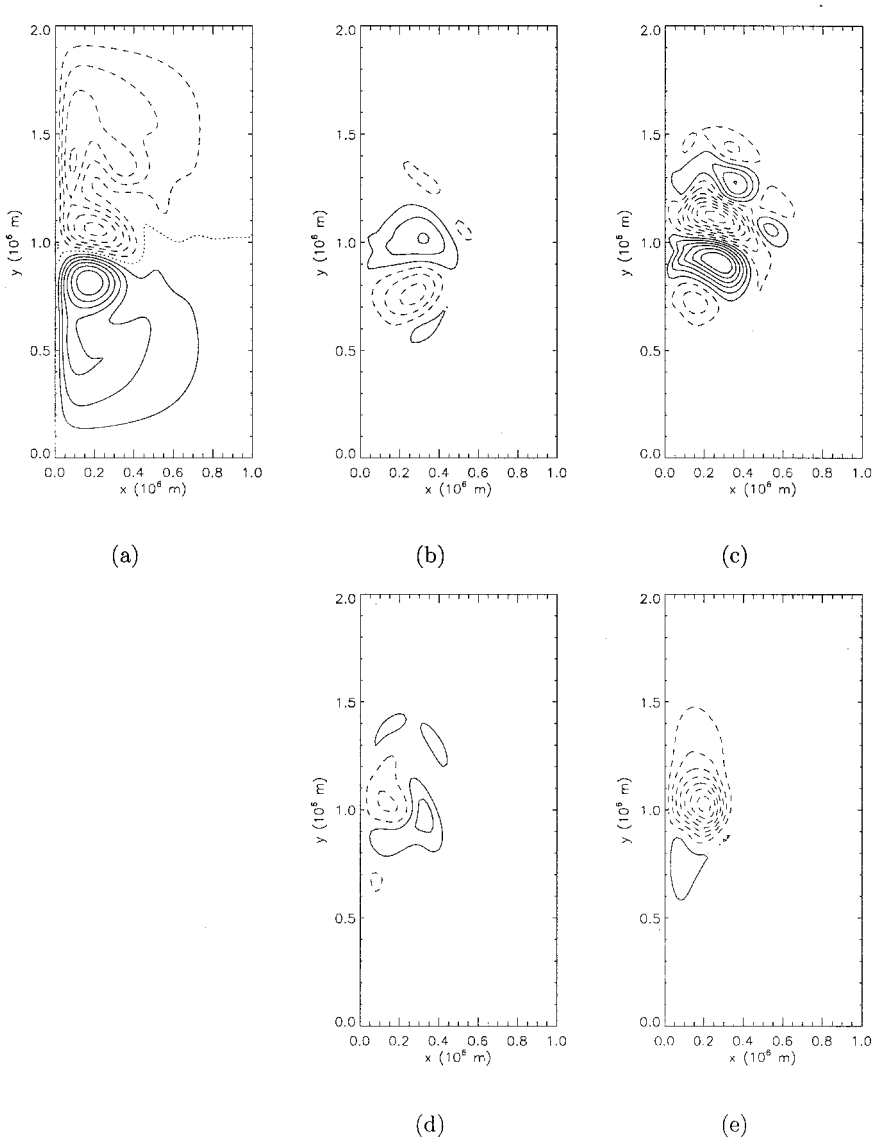

Figure 16. Panel (a) shows the upper layer streamfunction of the steady state at Hopf bifurcation H_3 in the case with the 'shelf + ridge' bottom topography of (11) at a wind stress of $\tau_0 = 7.8 \times 10^{-2}$ Pa. Panels (b) and (c) show the imaginary and real parts of the perturbation of the upper layer streamfunction and panels (d) and (e) of the lower layer streamfunction. The mode has a period of $\mathcal{P} = 26$ yr.

variance within the window (73%), has a similar pattern as in Figure 12. This confirms that this type of bottom topography induces a preference for the low-frequency mode. The main conclusion from this section is that the low-frequency mode is not solely characteristic for

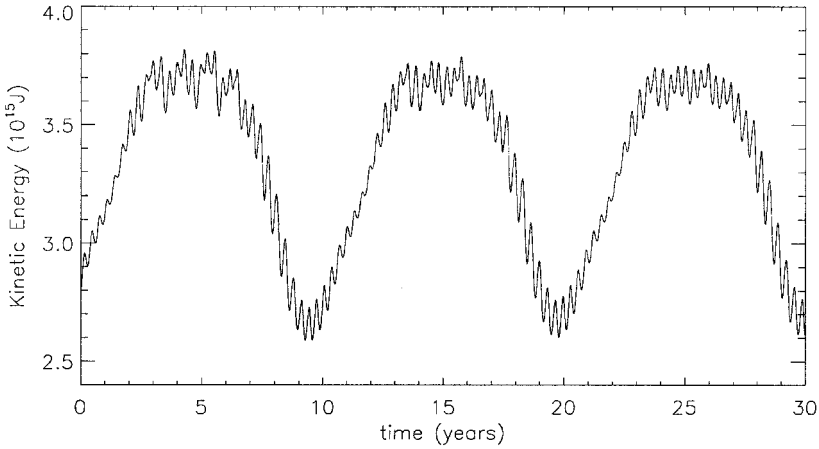

Figure 17. Time series of the basin integrated kinetic energy at a wind stress of $\tau_0 = 8.0 \times 10^{-2}$ Pa with the 'shelf + ridge' topography of (11).

the flat bottom case; that the period may be sensitive to the shape of the particular topography, but that it remains of decadal time scale.

4. Discussion

For a particular case, consisting of a wind-driven, two-layer, shallow-water flow in a small 1000 × 2000 km basin, a connection has been established between the modes destabilizing the steady states and low-frequency variability in the transient flow which is associated with the transitions between high- and low-energy states.

For the model here, the modes destabilizing at the first four Hopf bifurcations along the primary branch of steady solutions have oscillation periods in the order of several months. These modes are related either to baroclinic modes or to Rossby basin modes. The baroclinic modes have also been found in the two-layer quasi-geostrophic model (Dijkstra and Katsman, 1997) and are strongly related to those found in the classical Phillips model (Phillips, 1954), except that they are localized in the jet and have to satisfy the basin boundary conditions. Rossby basin modes have been found in many models of the double-gyre (Speich *et al.,* 1995; Dijkstra and Katsman, 1997; Chang *et al.,* 2001) and single-gyre (Sheremet *et al.,* 1997) wind-driven ocean circulation. The mechanism and time scale of the Rossby basin modes are easily related to the free Rossby basin modes in the inviscid case, propagating on a motionless background flow (Pedlosky, 1987).

At the fifth Hopf bifurcation, a low-frequency 'gyre' mode destabilizes, which has also been found in many modeling studies of the double-gyre circulation (Dijkstra and Katsman, 1997; Dijkstra and Molemaker, 1999; Simonnet *et al.,* 2001a). Contrary to the Rossby basin modes, the 'gyre' mode has no 'free' equivalent (Simonnet and Dijkstra, 2001). It originates from a (symmetry-breaking) shear instability which is unrelated to

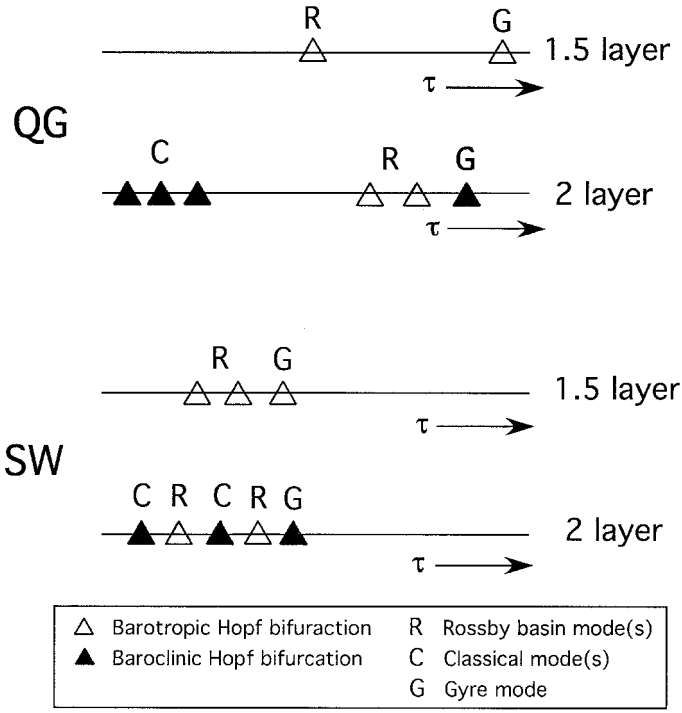

Figure 18. Schematic figure of the destabilized modes in bifurcation diagrams of different types of models.

baroclinic processes and Rossby wave dynamics. The gyre mode has an interannual oscillation period in the barotropic case, but here it appears to be modified by baroclinic processes, leading to a larger (decadal) oscillation period. An overview of the ordering and types of modes found in simplified models of the wind-driven circulation is presented (schematically) in Figure 18. In the two-layer shallow-water model, all the different modes in the spectrum destabilize close to each other in parameter space, contrary to the two-layer quasi-geostrophic model, which shows a strong separation of these modes. Therefore, in the two-layer shallow-water model interesting time-dependent behavior is already attained at relatively low forcing and can be analyzed near criticality.

Is this low-frequency behavior mainly associated with interactions of the high-frequency instabilities or with the destabilization of the low-frequency mode? The time mean state for the trajectory at $\tau_0 = 8.5 \times 10^{-2}$ Pa is not very different from that of the unstable steady state at H_5. Moreover, the spectrum for the basin integrated kinetic energy is not broad banded. Hence, the rectification of the mean state through the high-frequency instabilities is only weak and the (self-) interactions of the high-frequency modes cannot be responsible for the low-frequency variability. Therefore, the low-frequency mode is responsible for this behavior in the regime explored, as is also inferred from the dominant MSSA-pattern.

The dynamics associated with the destabilization of this mode strongly controls the time-dependent flow. This is not solely characteristic for the flat bottom case, because the presence of two specific types of bottom topography does not remove the 'gyre' mode from the spectrum, but causes the position of the Hopf bifurcation associated with this mode to be moved toward lower values of the wind stress forcing. Low-frequency variability found in other studies can probably also be associated with the presence of a 'gyre' mode. For example, in Katsman *et al.* (2000), the dynamical influence of a deep western boundary current is modeled in the lower layer of a quasi-geostrophic model. It was shown that low-frequency variability (associated with a similar pattern as the barotropic 'gyre' mode) becomes prominent in the time-dependent behavior as the strength of a deep western boundary current is increased.

Can the presence of such oscillatory 'gyre' modes explain the low-frequency variability of the wind-driven ocean circulation in the large-basin/high-forcing case (McCalpin and Haidvogel, 1996; Berloff and McWilliams, 1999)? Although it is impossible to demonstrate more rigourously, there are several arguments to support such a conjecture. We will go through these by discussing the deformation from the small-basin/low-forcing case, considered here, toward this (more) 'realistic' case.

(i) The 'gyre' modes still appear when a basin with a larger dimension is taken (Dijkstra and Molemaker, 1999) and they are even present in a basin with real North-Atlantic continental geometry (Schmeits and Dijkstra, 2001). The reason is that the presence of these modes is tightly coupled to the occurrence of multiple equilibria (Simonnet and Dijkstra, 2001), which are still present in shallow-water models of flows in larger basins. Only the (localized) structure of western boundary current/midlatitude jet system is important here, since this is the region where nonlinear processes are important, and not the total basin wide flow.

(ii) The 'gyre' modes will still appear on highly rectified mean states, as long as they are sufficiently asymmetric. In the high-forcing (or low-friction) case, many modes of the classes mentioned above (Chang *et al.,* 2001; Sheremet *et al.,* 1997) will be unstable. All modes except the 'gyre' mode will have relatively high frequencies and will strongly interact and rectify the mean state. As shown in Simonnet and Dijkstra (2001), the growth rate of the 'gyre' mode is dependent as the asymmetry of the rectified mean state, becoming larger as the asymmetry increases. The rectified mean states in low-friction cases still have an asymmetric structure (McCalpin and Haidvogel, 1996; Berloff and McWilliams, 1999), which indicates that one would still expect the 'gyre' modes to appear on these states. In fact, the low-frequency EOF pattern in Berloff and McWilliams (1999) (their Fig. 15) found in the high-friction/symmetrically-forced case has a similar structure as the 'gyre' mode. In this view, the effect of the high-frequency instabilities is only to rectify the mean state and to add noise to the flow, such that the low-frequency peak in the spectrum, which is associated with the high- and low-energy states and caused by the gyre mode, is broadened.

Although one cannot exclude that more complex dynamical phenomena, such as homoclinic or heteroclinic orbits play a role, the view above is elegant in that it is simple. The heart of the physics of the low-frequency variability can be traced back to a particular gyre mode and hence to the symmetry breaking shear instabilities. Since there is a distinct pattern of variability associated with each particular low-frequency mode, one may try to identify these in observations and output of high resolution ocean models.

Acknowledgments. This work was supported by the Netherlands Organization for Scientific Research (NWO) under a PIONIER grant to HD. All computations were performed on the CRAY C90 at the Academic Computing Centre (SARA), Amsterdam, The Netherlands within the project SC498. Use of these computing facilities was sponsored by the National Computing Facilities Foundation with financial support from NWO. We thank both referees for their comments on the first version of this paper.

REFERENCES

Asselin, R. 1972. Frequency filter for time integrations. Mon. Weath. Rev., *100,* 487–490.

Berloff, P. S. and J. C. McWilliams. 1999. Large-scale, low-frequency variability in wind-driven ocean gyres. J. Phys. Oceanogr., *29,* 1925–1949.

Bleck, R. and D. B. Boudra. 1981. Initial testing of a numerical ocean circulation model using a hybrid (quasi-isopycnic) vertical coordinate. J. Phys. Oceanogr., *11,* 755–770.

Cessi, P. and G. R. Ierley. 1995. Symmetry-breaking multiple equilibria in quasi-geostrophic, wind-driven flows. J. Phys. Oceanogr., *25,* 1196–1205.

Chang, K.-I., M. Ghil, K. Ide and C.-C. A. Lai. 2001. Transition to aperiodic variability in a wind-driven double-gyre circulation model. J. Phys. Oceanogr., *31,* 1260–1286.

Colin de Verdière, A. and T. Huck. 1999. Baroclinic instability: an oceanic wavemaker for interdecadal variability. J. Phys. Oceanogr., *29,* 893–910.

Cox, M. 1987. An eddy-resolving model of the ventilated thermocline: time-dependence. J. Phys. Oceanogr., *17,* 1044–1056.

Delworth, T. L. 1996. North Atlantic interannual variability in a coupled ocean-atmosphere model. J. Climate, *9,* 2356–2375.

Deser, C. and M. L. Blackmon. 1993. Surface climate variations over the North Atlantic ocean during winter: 1900–1989. J. Climate, *6,* 1743–1753.

Dijkstra, H. A. 2000. Nonlinear Physical Oceanography, Kluwer Academic Publishers, Dordrecht, The Netherlands, 480 pp.

Dijkstra, H. A. and C. A. Katsman. 1997. Temporal variability of the wind-driven quasi-geostrophic double gyre ocean circulation: Basic bifurcation diagrams. Geophys. Astrophys. Fluid Dyn., *85,* 195–232.

Dijkstra, H. A. and M. J. Molemaker. 1999. Imperfections of the North-Atlantic wind-driven ocean circulation: Continental geometry and wind stress shape. J. Mar. Res., *57,* 1–28.

Dijkstra, H. A., M. J. Schmeits and C. A. Katsman. 1999. Internal variability of the North Atlantic wind-driven ocean circulation. Surveys in Geophys., *20,* 463–503.

Holland, W. R. 1973. Baroclinic and topographic influences of the transport in the western boundary currents. Geophys. Fluid Dyn., *4,* 187–210.

Holland, W. R. and L. B. Lin. 1975. On the generation of mesoscale eddies and their contribution to the ocean general circulation I. A preliminary numerical experiment. J. Phys. Oceanogr., *5,* 642–657.

Huck, T., A. Colin de Verdière and A. Weaver. 1999. Interdecadal variability of the thermohaline circulation in box-ocean models forced by fixed surface fluxes. J. Phys. Oceanogr., *29,* 865–892.

Jiang, S., F.-F. Jin and M. Ghil. 1995. Multiple equilibria and aperiodic solutions in a wind-driven double gyre, shallow water model. J. Phys. Oceanogr., *25,* 764–786.

Katsman, C. A., S. S. Drijfhout and H. A. Dijkstra. 2000. The interaction of the Deep Western Boundary Current and the wind-driven gyres as a cause for low-frequency variability. J. Phys. Oceanogr., *31,* 2321–2339.

Kushnir, Y. 1994. Interdecadal variations in North Atlantic sea surface temperature and associated atmospheric conditions. J. Phys. Oceanogr., *7,* 141–157.

Latif, M. and T. Barnett. 1994. Causes of decadal climate variability over the North-Pacific and North-America. Science, *266,* 634–637.

Levitus, S. 2000. Warming of the world ocean. Science, *287,* 2225–2229.

McCalpin, J. D. and D. B. Haidvogel. 1996. Phenomenology of the low-frequency variability in a reduced gravity quasi-geostrophic double-gyre model. J. Phys. Oceanogr., *26,* 739–752.

McWilliams, J. C. 1996. Modeling the ocean general circulation. Ann. Rev. Fluid Mech., *28,* 215–248.

Miller, A. J., W. R. Holland and M. C. Hendershott. 1987. Open-ocean response and normal mode excitation in an eddy-resolving general circulation model. Geophys. Astrophys. Fluid Dyn., *37,* 253–278.

Pedlosky, J. 1987. Geophysical Fluid Dynamics, Springer-Verlag, NY, 710 pp.

—— 1996. Ocean Circulation Theory, Springer, NY, 450 pp.

Phillips, N. A. 1954. Energy transformations and meridional circulations associated with simple baroclinic waves in a two-level, quasi-geostrophic model. Tellus, *6,* 273–286.

Plaut, G. and R. Vautard. 1994. Spells of low-frequency oscillations and weather regimes in the northern hemisphere. J. Atmos. Sci., *51,* 210–236.

Primeau, F. W. 1998. Multiple equilibria of a double-gyre ocean model with super-slip boundary conditions. J. Phys. Oceanogr., *28,* 2130–2147.

Schmeits, M. J. and H. A. Dijkstra. 2001. Bimodality of the Kuroshio and the Gulf Stream. J. Phys. Oceanogr., (in press).

Sheremet, V. A., G. R. Ierley and V. M. Kamenkovich. 1997. Eigenanalysis of the two-dimensional wind-driven ocean circulation problem. J. Mar. Res., *55,* 57–92.

Simonnet, E. and H. A. Dijkstra. 2001. Spontaneous generation of low-frequency modes of variability in the wind-driven ocean circulation. J. Phys. Oceanogr., (in press).

Simonnet, E., M. Ghil, K. Ide, R. Témam and S. Wang. 2001a. Low-frequency variability in shallow-water models of the wind-driven ocean circulation. Part I: Steady-state solutions. J. Phys. Oceanogr., (submitted).

—— 2001b. Low-frequency variability in shallow-water models of the wind-driven ocean circulation. Part II: Time dependent solutions. J. Phys. Oceanogr., (submitted).

Speich, S., H. A. Dijkstra and M. Ghil. 1995. Successive bifurcations in a shallow-water model applied to the wind-driven ocean circulation. Nonlinear Proc. Geophys., *2,* 241–268.

Steward, W. J. and A. Jennings. 1981. A simultaneous iteration algorithm for real matrices. ACM Trans. Math. Software, *7,* 184–198.

Te Raa, L. A. and H. A. Dijkstra. 2001. Instability of the thermohaline ocean circulation on interdecadal time scales. J. Phys. Oceanogr., (in press).

Received: *22 November, 2000;* revised: *18 June, 2001.*